



First Detection of Radio Emission from the Intermediate-mass Black Hole in POX 52: Deep Multiband Observations with ATCA and VLA

Downloaded from: <https://research.chalmers.se>, 2025-04-03 05:10 UTC

Citation for the original published paper (version of record):

Yuan, Q., Guo, H., Gu, M. et al (2025). First Detection of Radio Emission from the Intermediate-mass Black Hole in POX 52: Deep Multiband Observations with ATCA and VLA. *Astrophysical Journal*, 980(1).
<http://dx.doi.org/10.3847/1538-4357/ada946>

N.B. When citing this work, cite the original published paper.



First Detection of Radio Emission from the Intermediate-mass Black Hole in POX 52: Deep Multiband Observations with ATCA and VLA

Qi Yuan^{1,2}, Hengxiao Guo², Minfeng Gu², Jamie Stevens³, Philip G. Edwards³, Yongjun Chen², Wenwen Zuo², Jingbo Sun^{2,4}, Jun Yang⁵, Paulina Lira⁶, Tao An², Renzhi Su⁷, Yuanqi Liu², Yijun Wang^{8,9}, Ning Chang¹⁰, Pengfei Jiang¹⁰, and Ming Zhang^{10,11,12}

¹ Changchun Observatory, National Astronomical Observatories, Chinese Academy of Sciences, Changchun 130117, People's Republic of China; yuanqi@cho.ac.cn

² Shanghai Astronomical Observatory, Chinese Academy of Sciences, 80 Nandan Road, Shanghai 200030, People's Republic of China; hengxiaoguo@gmail.com, gumf@shao.ac.cn

³ CSIRO Astronomy and Space Science, PO Box 76, Epping, NSW, 1710, Australia

⁴ University of Chinese Academy of Sciences, 19A Yuquan Road, 100049, Beijing, People's Republic of China

⁵ Department of Space, Earth and Environment, Chalmers University of Technology, Onsala Space Observatory, SE-43992 Onsala, Sweden

⁶ Departamento de Astronomía, Universidad de Chile, Casilla 36D, Santiago, Chile

⁷ Research Center for Astronomical Computing, Zhejiang Laboratory, Hangzhou 311100, People's Republic of China

⁸ School of Astronomy and Space Science, Nanjing University, 163 Xianlin Avenue, Nanjing 210023, People's Republic of China

⁹ Key Laboratory of Modern Astronomy and Astrophysics, Nanjing University, Ministry of Education, 163 Xianlin Avenue, Nanjing 210023, People's Republic of China

¹⁰ Xinjiang Astronomical Observatory, Chinese Academy of Sciences, 150 Science 1-Street, Urumqi 830011, People's Republic of China

¹¹ Key Laboratory of Radio Astronomy, CAS, 150 Science 1-Street, Urumqi 830011, People's Republic of China

¹² Xinjiang Key Laboratory of Radio Astrophysics, 150 Science 1-Street, Urumqi 830011, People's Republic of China

Received 2024 December 4; revised 2025 January 9; accepted 2025 January 9; published 2025 February 6

Abstract

We present the first multiband centimeter detection of POX 52, a nearby dwarf galaxy believed to harbor a robust intermediate-mass black hole. We conducted the deep observations using the Australia Telescope Compact Array (ATCA), spanning frequencies from 4.5 to 10 GHz, as well as the sensitive observations from the Karl G. Jansky Very Large Array (VLA) operating in its most extended A configuration at S band (2–4 GHz) and C band (4–8 GHz). In the ATCA observations, the source shows a compact morphology, with only one direction marginally resolved. The higher resolution of the VLA allowed us to slightly resolve the source, fitting it well with a two-dimensional Gaussian model. The detected radio emission confirms the presence of active galactic nucleus (AGN) activity, indicating either a low-power jet or AGN-driven winds/outflows. Our dual-epoch observations with ATCA and VLA, together with previous nondetection flux density upper limits, reveal radio emission variability spanning two decades. In addition, we find that POX 52 aligns well with the low-mass extension of the fundamental plane for high-accretion, radio-quiet massive AGNs.

Unified Astronomy Thesaurus concepts: [Intermediate-mass black holes \(816\)](#); [Radio continuum emission \(1340\)](#); [Seyfert galaxies \(1447\)](#); [Dwarf galaxies \(416\)](#)

1. Introduction

Intermediate-mass black holes (IMBHs), with masses of 10^2 – $10^6 M_{\odot}$ (M. Mezcua 2017), bridge the gap between stellar-mass BHs and supermassive BHs (SMBHs; $M_{\text{BH}} \geq 10^6 M_{\odot}$). As observations from the James Webb Space Telescope (JWST) push the discovery of first-generation quasars to earlier and earlier cosmic epochs (e.g., V. Kokorev et al. 2023), understanding how SMBHs formed has become an urgent problem in cosmology (R. Valiante et al. 2018). Detecting populations of IMBHs could provide constraints on these elusive black hole seeds. However, probing these seed BHs in the early Universe is beyond the reach of current observational capabilities.

Additionally, rapidly growing SMBHs at high redshifts quickly lose all trace of their origins. Fortunately, theoretical work suggests that observations of local, leftover IMBHs in dwarf galaxies may also provide crucial clues to understanding seeding processes, as these galaxies are relatively pristine and

have undergone fewer mergers and less accretion since their formation compared to their supermassive counterparts (M. Volonteri et al. 2008; S. van Wassenhove et al. 2010; K. Inayoshi et al. 2020). Therefore, confirming the IMBH nature serves as a first step in understanding SMBH formation history.

About two decades ago, NGC 4395 and POX 52 were considered two prototypical IMBH hosts in the local Universe, supported by multiwavelength evidence, including optical spectroscopic signatures (A. V. Filippenko & L. C. Ho 2003; A. J. Barth et al. 2004). With advancements in observational technology, the number of IMBH candidates has increased to hundreds. A growing body of research leverages multi-wavelength tracers, including optical spectroscopic diagnostics (J. E. Greene & L. C. Ho 2004; X.-B. Dong et al. 2012; A. E. Reines et al. 2013; H.-Y. Liu et al. 2018; S. Salehirad et al. 2022), optical/X-ray variability (V. F. Baldassare et al. 2018; P. Lira et al. 2020; N. Kamizasa et al. 2012), coronal lines (E. J. Wasleske & V. F. Baldassare 2024), mid-infrared color diagnostics (S. Satyapal et al. 2014; L. F. Sartori et al. 2015), and radio/X-ray emissions (A. E. Reines et al. 2020; A. J. Sargent et al. 2022), to explore active IMBHs within low-mass/dwarf galaxies. It is important to note that selection biases exist among IMBH candidates identified across different

bands (A. Askar et al. 2023; E. J. Wasleske & V. F. Baldassare 2024). Thus, insightful multiband follow-up studies can help confirm their IMBH nature and enhance our understanding of the physics and characteristics of this population.

The two most reliable IMBH candidates, in the dwarf galaxies NGC 4395 and POX 52, exhibit very different host properties and accretion modes. NGC 4395 is a late-type, bulgeless spiral dwarf galaxy at $z = 0.00106$ (~ 4.5 Mpc). Reverberation mapping of its H α line indicates a BH mass of $\sim 1.7 \times 10^4 M_{\odot}$, with an Eddington ratio around 0.06 (J.-H. Woo et al. 2019; H. Cho et al. 2021; S. Pandey et al. 2024). In contrast, POX 52 (J1202–2056, at $z = 0.021$, or ~ 90 Mpc) is a dwarf elliptical galaxy lacking any obvious spiral, disklike structure, or clumps and accreting close to the Eddington limit (A. J. Barth et al. 2004). The estimated single-epoch BH mass is $\sim 1.6 \times 10^5 M_{\odot}$, based on Keck spectroscopic observations (A. J. Barth et al. 2004). POX 52 has been extensively studied in multiband observations (A. J. Barth et al. 2004; C. E. Thornton et al. 2008; T. Kawamuro et al. 2024) and exhibits significant optical variability and dust echo, offering the potential for accurate BH mass estimation through reverberation mapping techniques (J. B. Sun et al. 2025, in preparation).

Radio properties are crucial for studying BHs and can provide independent evidence of AGN activity, as well as insights into the characteristics of IMBHs. In the radio regime, NGC 4395 has been observed across various frequencies using interferometer arrays with different angular resolutions to investigate its radio origins (P. Saikia et al. 2018; J. Yang et al. 2022; P. Nandi et al. 2023). Research has progressed from initial explorations of radiation properties on the arcsecond scale to subarcsecond detections, which could determine whether there is a sub-parsec-scale continuous or episodic jet tracing the accreting IMBH (see J. Yang et al. 2022, 2023, and references therein). In contrast, no significant radio emission from POX 52 has been detected before this work. Previous radio observations employed the historical Very Large Array (VLA; A. R. Thompson et al. 1980) in its A configuration with the C band (J. E. Greene et al. 2006; sensitivity: $26 \mu\text{Jy beam}^{-1}$) and the VLA Sky Survey (VLASS; M. Lacy et al. 2020) Epoch 1, 2, and 3 Quick Look (Y. A. Gordon et al. 2021; sensitivities: 155, 130, and $140 \mu\text{Jy beam}^{-1}$, respectively). The failure to detect radio emission from POX 52 may be attributed to sensitivity limitations, its inherently faint nature—potentially linked to the anticorrelation between accretion rate and relative radio strength compared to the optical (see L. C. Ho 2002)—or the possibility that previous observations performed during a radio quiescent state (J. E. Greene & L. C. Ho 2006). As one of the most promising IMBH candidates, and in contrast to the low accretion state of NGC 4395, it serves as a representative for high-accretion sources. Thus, high-sensitivity deep observations are essential.

This paper reports our first multiband radio detections of POX 52 and characterizes its radio properties. The layout is as follows: In Section 2, we describe our observations and data reduction. We present the result in Section 3 and discuss our findings in Section 4. We draw our conclusions in Section 5. Throughout the paper, we use the cosmological parameters $\Omega_m = 0.27$, $\Omega_{\Lambda} = 0.73$, and $H_0 = 71 \text{ km s}^{-1} \text{ Mpc}^{-1}$. In this adopted Λ CDM cosmology, the angular scale at the source redshift $z = 0.021$ is $419 \text{ pc arcsec}^{-1}$.

2. Observations and Data Reduction

2.1. ATCA observations

POX 52 was observed with the Australia Telescope Compact Array (ATCA) in its 4 cm band, using the Compact Array Broadband Backend (CABB) system (W. E. Wilson et al. 2011). The observations were made in the 6 C configuration on 2022 November 18 (Program ID: C3510) and were carried out with two 2 GHz wide intermediate frequencies (IFs) of 4.5–6.5 GHz (centered at 5.5 GHz) and 8–10 GHz (centered at 9 GHz). PKS B1934–638 was used as a bandpass and flux density calibrator, while 1143–245 was used as a complex gain calibrator. The data reduction was carried out with the software Miriad (R. J. Sault et al. 1995), following the standard procedure.

Automatic radio frequency interference flagging was performed using the task *pgflag* before calibration. In total, 12.7% of the 5.5 GHz band and 18.5% of the 9 GHz band was flagged as bad. Standard calibration involved bandpass and flux density calibration on PKS B1934–638 using the Miriad tasks *mfc* and then *gpcal*, and this was applied to the gain calibrator 1143–245. Time-varying gains and polarization leakage calibration were done using the task *gpcal* on 1143–245, and these gains were transferred and applied to the source before imaging.

Imaging was performed using the tasks *invert*, *mfclean*, and *restor*, to create two continuum images, one for each of the IFs, using multifrequency synthesis. Images were made in Stokes *I*, with a Briggs visibility weighting robustness parameter of -1 . Cleaning with *mfclean* was done with both the Clark and Hogbom algorithms down to a depth of $40 \mu\text{Jy}$ in both IFs. Images were restored with a Gaussian synthesized beam of $3''.084 \times 0''.9318$ with a position angle of -0.574 for the 5.5 GHz image and $2''.013 \times 0''.6068$ with a position angle of -0.578 for the 9 GHz image. The central 10% of the 5.5 GHz image has an rms noise level of $11.4 \mu\text{Jy}$, while the 9 GHz image has an rms noise level of $8.2 \mu\text{Jy}$. Source flux density fits were made using the task *imfit*.

2.2. VLA Observations

Our target was also observed with the VLA in the most extended A configuration in 2023 July 28 (Program ID: 23A-163). Continuum observations were carried out at S band with 2×1 GHz basebands centered at 3 GHz and at C band with 2×2 GHz basebands centered at 6 GHz. For better *u-v* coverage, we alternated between the two bands, repeating this sequence three times during the overall scheduling block (SB). The first two sub-SBs began with observations of a flux calibrator (3C 286) and then iterated between observing a complex gain calibrator (PKS J1159–2148) and the target source, ending with the observation of the former. The third sub-SB mirrored the mode of the preceding two but omitted the flux scale observation. The raw data were reduced with the Common Astronomy Software Applications (CASA) package, version 6.5.4 (J. P. McMullin et al. 2007), with additional manual flagging.

The calibrated visibilities were imaged using the CLARK deconvolution algorithm (B. G. Clark 1980) CASA task TCLEAN. The CLEAN map, as shown in Figure 1, was reconstructed by adopting the natural weighting to optimize the sensitivity. The background noise level is obtained by examining pixels well away from the source, executed by the

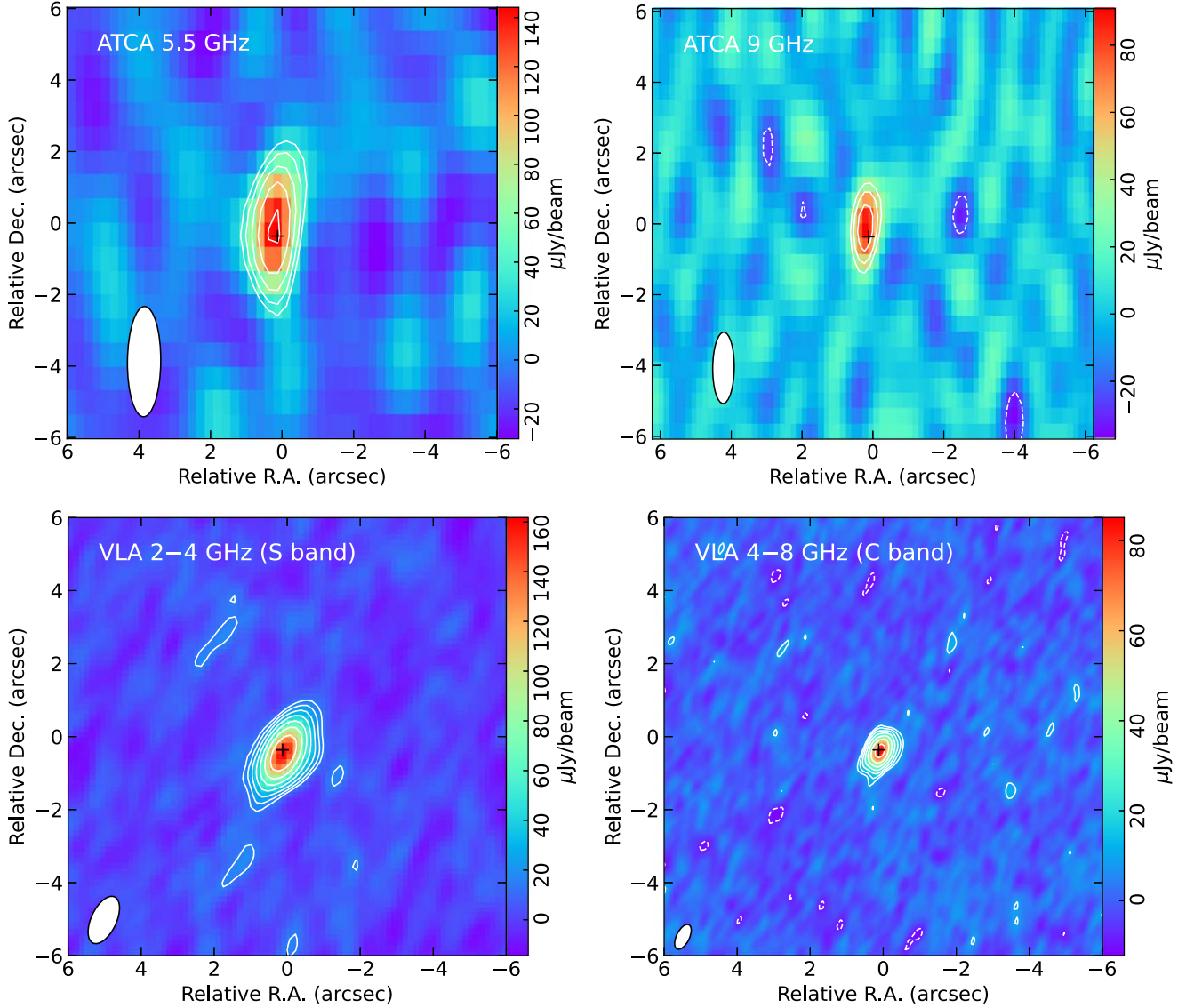


Figure 1. Naturally weighted CLEAN map of POX 52 observed by ATCA and VLA, centered at the radio positions obtained by model fitting. Contours in the map are plotted at multiples of $-1, 1, \sqrt{2}, 2, 2\sqrt{2}, 4, 4\sqrt{2}, 8, 8\sqrt{2}$, and $16 \times 3\sigma$, where σ is the local rms noise. The off-source background noise of each observation is $11.4, 8.2, 4.8$, and $3.0 \mu\text{Jy beam}^{-1}$, respectively. The white ellipses in the lower left corner of each panel represent the FWHM of the restoring beam. The plus sign indicates the optical center obtained from Gaia DR3 (Gaia Collaboration et al. 2023).

Table 1
ATCA and VLA Observations

Telescope	Frequency (GHz)	$t_{\text{on-source}}$ (hr)	Peak Intensity ($\mu\text{Jy beam}^{-1}$)	Integrated Flux Density (μJy)	Synthesized Beam (arcsec, arcsec, deg)	Size (arcsec, arcsec)	rms ($\mu\text{Jy beam}^{-1}$)	SNR	\mathcal{F}
(1)	(2)	(3)	(4)	(5)	(6)	(7)	(8)	(9)	(10)
ATCA	4.5–6.5	9	153 ± 12	260 ± 31	(3.08, 0.93, -0.57)	unresolved	11.4	13	...
ATCA	8–10	9	95 ± 9	160 ± 22	(2.01, 0.61, -0.58)	unresolved	8.2	12	...
VLA	2–4 (S band)	0.99	157 ± 5	229 ± 11	(1.40, 0.69, -25.15)	(0.82, 0.50)	4.8	32	1.46
VLA	4–8 (C band)	0.97	82 ± 3	146 ± 8	(0.74, 0.35, -26.16)	(0.44, 0.41)	3.0	27	1.81

Note. Column (1): radio interferometer. The ATCA and VLA observations were performed on 2022 November 18 and 2023 July 28, respectively. Column (2): observing frequency. Column (3): integration time on source. Column (4): peak intensity. Column (5): integrated flux density. Column (6): synthesized beam. Column (7): the source sizes deconvolved from the beam. Column (8): rms noise level. Column (9): signal-to-noise ratio. Column (10): ratio between integrated flux and peak flux (\mathcal{F}).

task IMSTAT. In addition to the maps with natural weighting, we also produced lower-resolution u - v -tapered C-band 4–6 GHz and 6–8 GHz maps that match the resolution of the S band for spectral shape analysis only. It is

implemented by splitting the total bandwidth of the C band into two portions and assigning lower weights to the visibility corresponding to small scales (i.e., long baselines).

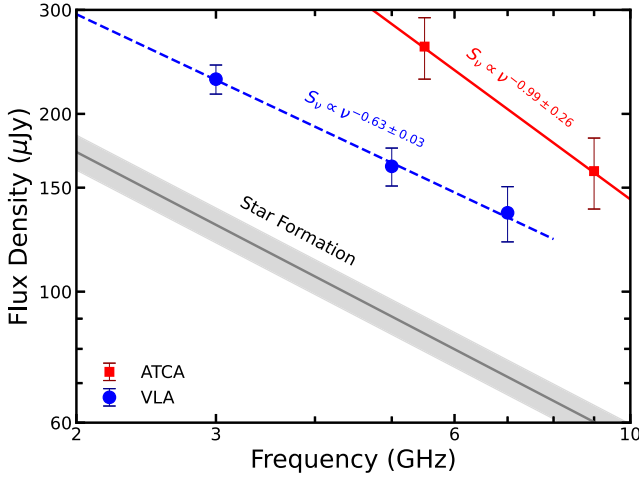


Figure 2. The radio spectra of POX 52. The red squares and blue circles represent ATCA and VLA observations, respectively. The red solid and blue dashed lines show the best-fitting power-law spectra for ATCA and VLA observations, respectively. The gray solid line denotes the anticipated flux density values for star formation, while the surrounding gray shaded region reflects the associated uncertainty in the expected flux density due to the uncertainty in the SFR.

We utilized the CASA task IMFIT to acquire source parameters, including integrated flux density, peak intensity, and size. The final observation image in each band can be well fitted by a single 2D elliptical Gaussian component. The source information and corresponding errors are listed in Table 1; the errors are derived from the uncertainty estimates in the IMFIT model fitting combined with the 3% limit in the flux calibration (R. A. Perley & B. J. Butler 2017).

3. Results and Analysis

3.1. Radio Emission and Spectral Index

POX 52 is detected in both bands in ATCA and VLA observations with signal-to-noise ratios (SNRs) ≥ 10 . The ATCA and VLA CLEAN maps are shown in Figure 1, and the radio emission is consistent with the optical center provided by Gaia Data Release 3 (DR3; Gaia Collaboration et al. 2023). We calculated the spectral index (α), which is defined as the power-law spectrum $S_\nu \propto \nu^{-\alpha}$, where S_ν is the integrated flux density at frequency ν . Through a nonlinear least-squares minimization, we obtained a best-fit spectral index of 0.63, with an uncertainty of 0.03, for the VLA S-band and u - v -tapered C-band observations. For ATCA observations, which include only two flux density values, the two-point spectral index α is transformed into $\alpha = \frac{\log(S_1/S_2)}{\log(\nu_1/\nu_2)}$, with its uncertainty estimated as $\sqrt{(\sigma_{f_1}/S_{f_1})^2 + (\sigma_{f_2}/S_{f_2})^2} / \ln(f_2/f_1)$, where $\sigma_{f_{1,2}}$ and $S_{f_{1,2}}$ represent the uncertainties and the flux density at the two frequencies (L. C. Ho & J. S. Ulvestad 2001). The spectral index derived from the ATCA observation is 0.99 ± 0.26 . Figure 2 shows the radio spectra of POX 52.

According to the conventional classification of a steep spectrum ($\alpha \geq 0.5$), a flat spectrum ($0 \leq \alpha < 0.5$), and an inverted spectrum ($\alpha < 0$) (e.g., F. Panessa & M. Giroletti 2013), our target falls into the category of steep spectra in both ATCA and VLA observations, though with different angular resolution. This spectrum is significantly steeper than expected for thermal emission ($\alpha \sim 0.1$) or a self-absorbed jet base ($\alpha \sim 0$), indicating optically thin synchrotron emission.

3.2. Radio Loudness

The classification of AGNs into radio-quiet and radio-loud categories is used to characterize the strength of their radio emissions, reflecting the diverse underlying physical processes driving these emissions. The traditional radio-optical radio-loudness is defined as $\mathcal{R}_O = L_{5\text{GHz}}/L_{4400\text{\AA}}$ (K. I. Kellermann et al. 1989), where $L_{5\text{GHz}}$ and $L_{4400\text{\AA}}$ are the radio and optical flux densities at 5 GHz and 4400 Å in the rest frame, respectively. The rest-frame $L_{4400\text{\AA}}$ is obtained from the observed spectrum in A. J. Barth et al. (2004). We revisited the VLA C-band observations, dividing them into two 2 GHz basebands (4–6 GHz and 6–8 GHz) to obtain an accurate flux density at 5 GHz. This yielded a radio-loudness (\mathcal{R}_O) estimate of 0.57 for this source.

Regarding the radio-X-ray definition, $\mathcal{R}_X = L_R/L_X$, where L_R is the radio luminosity at 5 GHz and L_X is the integrated luminosity between 2 and 10 keV (Y. Terashima & A. S. Wilson 2003). The X-ray luminosity of POX 52, obtained from T. Kawamuro et al. (2024), is $\sim 10^{42} \text{ erg s}^{-1}$. The radio luminosity at 5 GHz is estimated by

$$L_R = \nu L_\nu = \nu f_\nu \frac{4\pi D_L^2}{(1+z)^{1+\alpha}}, \quad (1)$$

where α is the spectral index based on our VLA observation, f_ν is the integrated flux density at 5 GHz, and D_L is the luminosity distance. The L_R at 5 GHz is estimated to be $10^{36.92} \text{ erg s}^{-1}$, resulting in $\mathcal{R}_X = 10^{-5.08}$.

According to the traditional radio-quiet criterion based on either the radio-optical ($\mathcal{R}_O < 10$; K. L. Visnovsky et al. 1992; K. I. Kellermann et al. 1994) or radio-X-ray ($\mathcal{R}_X < 10^{-2.755 \pm 0.015}$; F. Panessa et al. 2007) ratio, the source is thus classified as radio-quiet by both criteria.

3.3. Brightness Temperature

The brightness temperature (T_b) of the fitted Gaussian component can be calculated using the following formula (Y. Y. Kovalev et al. 2005):

$$T_b = 1.22 \times 10^{12} \frac{f(1+z)}{\theta_{\text{maj}} \theta_{\text{min}} \nu_{\text{obs}}^2} \text{ K}, \quad (2)$$

where z is the source redshift, f is the integrated flux density of the fitted Gaussian component in Jy, θ_{min} and θ_{maj} are the FWHM dimensions of the Gaussian in mas, and ν_{obs} is the observing frequency in GHz. We estimated T_b using the highest-frequency subband (6–8 GHz) from the VLA C-band observation since it provides the highest spatial resolution in our observations. The estimated T_b at 7 GHz is $\sim 10^2 \text{ K}$. Note that the brightness temperature estimation for this source only serves as a lower limit, given that the measured angular diameters are below the nominal angular resolution.

3.4. Radio Morphology

For the ATCA observations, we could not deconvolve the source from the synthesized beam, suggesting that the source might be marginally resolved along one direction. In contrast, the high-resolution VLA observations can reveal finer morphological structures on smaller angular scales. To determine whether our source is resolved, we calculate the ratio of integrated flux to peak flux (\mathcal{F}), which serves as a

direct indicator of the radio source's extension (I. Prandoni et al. 2000; M. Bondi et al. 2003). The \mathcal{F} is characterized by the equation (M. T. Huynh et al. 2005)

$$\mathcal{F} = \frac{S_{\text{int}}}{S_{\text{peak}}} = \frac{\theta_{\text{maj}}\theta_{\text{min}}}{b_{\text{maj}}b_{\text{min}}}, \quad (3)$$

where θ_{maj} and θ_{min} represent the FWHM of the Gaussian component fitted, while b_{maj} and b_{min} denote the FWHM of the synthesized beam. According to the criterion provided by I. Prandoni et al. (2000), a source is considered resolved if $\mathcal{F} > 1.05 + \frac{10}{(\text{SNR})^{1.5}}$. For the VLA S and C bands, the \mathcal{F} values of 1.46 and 1.81 exceed the predicted thresholds of 1.11 and 1.12, given the corresponding SNRs of 32 and 27. Thus, we infer that the radio emission observed by VLA in each frequency band is resolved, albeit only slightly.

4. Discussion

4.1. Origin of the Compact Radio Emission

The interpretation of radio spectra in AGNs depends on various contributing components, which complicates identifying the dominant emission mechanism. For powerful radio-loud AGNs, a flat radio spectrum is typically considered to be dominated by the central compact radio core, while a steep radio spectrum indicates dominance by extended structures such as jets or lobes (J. J. Condon 1992). In radio-quiet AGNs, however, the situation is more complex, as the detected radio emission can originate from a variety of mechanisms, including star formation, AGN-driven winds, free-free emission from photoionized gas, low-power jets, and coronal activity from the innermost accretion disk (F. Panessa et al. 2019). Although we have some understanding of the radiative mechanisms of AGNs, the radio emission processes of low-mass AGNs are still poorly understood. A statistical analysis by J.-Z. Wu et al. (2024) reveals an unexpectedly high radio-loud fraction (>60%) in their low-mass AGN sample, suggesting that substantial radio emissions may originate from star formation within their host galaxies or that the radio-loudness is biased by the low luminosities characteristic of these low-mass AGNs. Therefore, it is essential to consider the contributions from the host galaxies thoroughly before making definitive conclusions.

4.1.1. Confirmation of AGN Activity

To rigorously evaluate the potential star formation contribution to the observed radio emission, we performed a comprehensive multiband analysis:

Radio-based SFR estimates. We calculate the expected monochromatic luminosity at 1.4 GHz based on the estimator from R. C. Kennicutt & N. J. Evans (2012):

$$\log L_{1.4\text{ GHz}} (\text{erg s}^{-1} \text{ Hz}^{-1}) = \log \text{SFR} (M_{\odot} \text{ yr}^{-1}) + 28.2, \quad (4)$$

which also incorporates the star formation rate (SFR) calibration from E. J. Murphy et al. (2011). The $\text{SFR} = 0.15 \pm 0.01 M_{\odot} \text{ yr}^{-1}$, derived from UV-IR spectral energy distribution (SED) fitting (T. Kawamuro et al. 2024). This results in an expected flux density of $222 \pm 14.8 \mu\text{Jy}$ at 1.4 GHz given the SED-based SFR. By extrapolating this flux density to the 2–10 GHz range using a power-law slope of $\alpha = 0.7$, a typical value for star-formation-driven emissions (J. J. Condon 1992; F. Panessa et al. 2019), we find that the

expected radio emission from star formation is significantly lower than the observed flux densities in both the ATCA and VLA data in Figure 2.

Radio spectral properties. While the measured spectral index ($\alpha \sim 0.63$) is similar to that expected from star formation ($\alpha \sim 0.7$; J. J. Condon 1992), the compact morphology (<1 kpc) differs from the extended radio emission typically associated with star formation (on several kiloparsec scales; see E. J. Murphy et al. 2012).

Multiband diagnostics. (a) The Baldwin, Phillips, and Terlevich (BPT) diagnostic ratios [O III]/H β and [N II]/H α place POX 52 firmly in the AGN region (R. R. Ludwig et al. 2012). (b) The mid-IR colors from the Wide-field Infrared Survey Explorer (WISE; $W_1 - W_2 = 0.86$) are consistent with AGN emission (D. Stern et al. 2012). (c) The observed X-ray luminosity ($L_X \sim 10^{42} \text{ erg s}^{-1}$) is two orders of magnitude higher than expected from star formation alone ($L_{X,\text{SF}} \approx 10^{40} \text{ erg s}^{-1}$ for $\text{SFR} = 0.15 M_{\odot} \text{ yr}^{-1}$, following B. D. Lehmer et al. 2016).

Host galaxy properties. Hubble Space Telescope imaging reveals that POX 52 is a dwarf elliptical galaxy lacking spiral arms or prominent star-forming regions (C. E. Thornton et al. 2008). The stellar population analysis indicates a predominantly old stellar population with mean age >5 Gyr (A. J. Barth et al. 2004).

Temporal characteristics. The observed radio variability on monthly timescales (Section 4.1.3) cannot be explained by star formation (A. Wang et al. 2023), which typically varies on much longer timescales (>100 yr; J. J. Condon 1992).

Therefore, based on our quantitative analysis of the star-forming contributions and above multiband evidence, we conclude that the observed radio emission in POX 52 predominantly originates from AGN activity.

4.1.2. The Origin of the AGN Activity

Although we have ruled out star formation as the origin of the radio emission, there are still multiple mechanisms by which AGNs could generate this emission, including coronal activity, winds/outflows, and jets. Distinguishing among these possibilities is very challenging given the limited resolution.

While the ratio of L_R to L_X appears consistent with the Güdel-Benz relation (M. Guedel & A. O. Benz 1993) for coronal emission, two factors argue against a coronal origin: (1) The coronal component originates from the innermost region surrounding the BH, spanning a range of approximately $10R_g - 10,000R_g$ (Schwarzschild radius; equivalent to 10^{-7} to 10^{-4} pc for a $10^5 M_{\odot}$ BH; F. Panessa et al. 2019). In contrast, our observed radio emission is resolved on a scale of 100 pc in VLA observations, which is orders of magnitude larger than the typical size of a corona. (2) The steep spectrum is inconsistent with the flat or inverted spectra that are typically associated with coronae (I. Raginski & A. Laor 2016).

The steep-spectrum component observed could be attributed to optically thin synchrotron emission, potentially dominated by plasma blobs within a subrelativistic jet or an AGN wind/outflow (A. Laor et al. 2019). In the observations of AGNs hosting SMBHs, jets typically extend over hundreds of parsecs, whereas outflows can span thousands of parsecs (F. Panessa et al. 2022). However, these structures tend to be more compact in the IMBH regime. Thus, it remains challenging to definitively conclude whether the observed radio emission originates from a jet, an outflow, or a combination of both,

although the elliptical components in VLA maps correspond to a physical scale of several hundred parsecs (see Table 1).

4.1.3. Radio Variability

As shown in Figure 2, the observed radio emission detected by ATCA is higher than that in VLA in the overlapping frequency. This discrepancy could be due to the VLA's higher angular resolution resolving out diffuse or extended emission detected by ATCA, or it might indicate real variability in the radio emission.

To verify the resolution scenario, we employed 10 short-baseline telescopes from the VLA to conduct mapping and model fitting. In this configuration, the major and minor axes of the synthesized beam are larger than those obtained with ATCA, namely a lower angular resolution compared to that of ATCA. Consequently, the VLA should have captured the diffuse or extended emission observed by ATCA. However, we found that the peak intensity and integrated flux densities at 5 GHz ($f_{\text{peak}} = 138 \pm 12 \mu\text{Jy beam}^{-1}$ and $f_{\text{int}} = 158 \pm 26 \mu\text{Jy}$) are still lower than those measured by ATCA in Table 1, indicative of the short-term AGN variability over the 8 months between ACTA and VLA observations. Moreover, an upper limit of $78 \mu\text{Jy}$ was reported in VLA's A configuration C-band observations in 2004 (C. E. Thornton et al. 2008), further confirming long-term radio variability over two decades.

4.2. The Radio Detections in Low-mass AGNs

Radio detections of low-mass AGNs remain rare owing to their faint and weak radio emission. A well-studied case is NGC 4395, with the angular resolution from subarcsecond (e.g., $0''.29 \times 0''.26$) to milliarcsecond scales (e.g., $3.13 \times 0.95 \text{ mas}$) (P. Saikia et al. 2018; J. Yang et al. 2022). VLA observations at 12–18 GHz (beam: $0''.13 \times 0''.12$) reveal an elongated structure with a total flux density of approximately $370 \mu\text{Jy}$; however, it turns out to be nuclear shocks likely formed by the IMBH's episodic ejection or wide-angle outflow rather than the core-jet in the milliarcsecond scale (J. Yang et al. 2022, 2023). Extending to other low-mass AGNs with pointing observations, most of the sub-arcsecond-scale deep observations show “compact” structure, namely a single component source, unresolved or slightly resolved (E. M. Cackett et al. 2014; K. Nyland et al. 2022; J. D. Paul et al. 2024).

Leveraging a comprehensive wide-field radio survey, L. Qian et al. (2018) and J.-Z. Wu et al. (2024) successfully identified radio counterparts for 151 optically selected low-mass AGNs, cataloged as 132 compact and 19 extended sources, based on a previous low-mass AGN catalog (X.-B. Dong et al. 2012; H.-Y. Liu et al. 2018). This identification was achieved by integrating data from Square Kilometer Array (SKA) pathfinders such as the LOFAR Two-meter Sky Survey (LoTSS; T. W. Shimwell et al. 2017, 2019, 2022), the Apertif-shallow survey (E. A. K. Adams et al. 2025, in preparation), and the VLASS Epoch 1 Quick Look, as well as through deep mining of data from the Faint Images of the Radio Sky at Twenty cm survey. This effort has quadrupled the number of known low-mass AGNs with radio counterparts, thereby establishing a solid foundation for future high-frequency observational studies.

4.3. The Fundamental Plane of Black Hole Activity

Accretion, outflows, and jets are prevalent across a wide range of astrophysical systems, varying in size, mass scale, and environmental conditions (R. M. T. Connors 2017). Over the past few decades, we have learned that BH accretion seems to be a scale-invariant process from X-ray binaries to SMBHs, thus establishing the empirical relation linking an accreting BH's mass (M_{BH}), radio luminosity (L_R), and X-ray luminosity (L_X), known as the fundamental plane of BH activity (A. Merloni et al. 2003; H. Falcke & S. Markoff 2004; D. O. Richstone et al. 2009; F. Yuan et al. 2009; R. M. Plotkin et al. 2012; E. M. Cackett et al. 2014; N. Chang et al. 2021; Y. Wang et al. 2024). This relationship has been thoroughly explored from the stellar-mass to the SMBH regimes, significantly enhancing our understanding of the underlying physics of BH accretion and jet dynamics. However, the application of this fundamental plane to IMBHs remains largely unexplored (T. J. Maccarone 2004; K. Nyland et al. 2022), and it is still unclear whether IMBHs conform to this empirical relation.

Observational evidence indicates that radio-quiet and radio-loud AGNs have distinct fundamental planes (R. Wang et al. 2006; Z.-Y. Li et al. 2008; L. G. C. Bariuian et al. 2022). Moreover, for both types of AGNs, the fundamental plane shows a significant dependence on the Eddington ratio (as summarized in Y. Wang et al. 2024). Thanks to the X-ray data and deep radio observations (E. M. Cackett et al. 2014; J. D. Paul et al. 2024) of 15 high Eddington ratio ($0.1 < \lambda_{\text{Edd}} < 1$; $\langle \lambda_{\text{Edd}} \rangle = 0.37$), radio low-mass AGNs, we can extend the fundamental plane to the IMBH regime, together with POX 52 ($\lambda_{\text{Edd}} \sim 0.5$, A. J. Barth et al. 2004; C. E. Thornton et al. 2008).

Given the limited size of our sample, the considerable uncertainties of BH masses, and the need for refined radio and X-ray luminosity measurements, we avoid deriving new relationships in our work. Instead, we simply check for consistency with an existing empirical relation described by Z.-Y. Li et al. (2008), which was established for a sample of 227 broad-line AGNs. Similar to our sample, this AGN sample is radio-quiet with an average Eddington ratio of 0.3.

Our findings, illustrated in Figure 3, demonstrate that POX 52, along with approximately half of the low-mass radio-quiet AGNs, follows the fundamental plane of supermassive AGNs as detailed in Z.-Y. Li et al. (2008), which share similar Eddington ratios ranging from 0.1 to 1, albeit with some outliers.

These deviations could stem from several factors: potentially overestimated radio emissions in low-mass AGNs due to additional contributions such as star formation (X. Yang & J. Yang 2023); underestimations of BH mass, considering a ~ 0.5 dex uncertainty based on the single-epoch spectrum (Y. Shen 2013); the nonsimultaneous multiband measurements; or intrinsic discrepancies. The fundamental plane sheds important light on the accretion physics and X-ray emission origins of central engines; our results suggest that the accretion and jet processes may be comparable across accreting systems with different BH masses, given a similar Eddington ratio, within the radio-quiet AGN population.

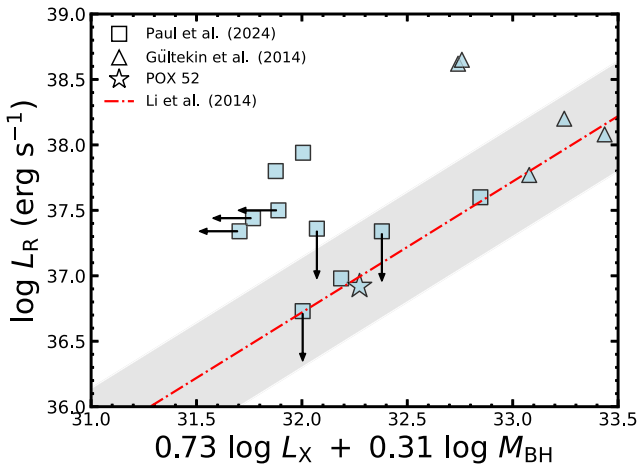


Figure 3. The IMBH candidates in the fundamental plane of BH activity. The red dashed–dotted line represents the best fit for a sample of 227 high Eddington ratio ($\bar{\lambda}_{\text{Edd}} = 0.3$) radio-quiet broad-line AGNs (Z.-Y. Li et al. 2008), with the shaded area indicating the 1σ uncertainty (0.42 dex) in the L_R direction. Squares and triangles denote 15 radio-quiet, low-mass AGNs with Eddington ratios greater than 0.1 and BH masses in the range $10^{5.5} M_{\odot} < M_{\text{BH}} < 10^{6.5} M_{\odot}$, respectively. For this comparison sample, we obtained values for the 5 GHz radio luminosity, 2–10 keV X-ray flux, BH mass, and Eddington ratio from the literature (J. E. Greene & L. C. Ho 2007; E. M. Cackett et al. 2014; J. D. Paul et al. 2024).

5. Conclusions

Our discovery of radio emission from POX 52 represents significant progress in the study of IMBHs and AGN physics. This first successful radio detection of one of the most promising nearby IMBH candidates provides crucial evidence for AGN activity in the IMBH regime, while demonstrating the feasibility of detecting radio emission from high Eddington ratio IMBHs. The detection enables direct comparison with SMBH systems, bridging a critical gap in our understanding of BH physics across the mass scale. The main conclusions are as follows:

1. The detailed characterization of POX 52’s radio properties has revealed several important physical insights. The steep spectrum (VLA: $\alpha = 0.63 \pm 0.03$; ATCA: $\alpha = 0.99 \pm 0.26$) clearly indicates the presence of optically thin synchrotron emission, while the observed radio variability on monthly timescales provides new constraints on emission mechanisms. The deconvolved angular sizes of the elliptical Gaussian components fitted in the VLA CLEAN maps favor the low-power jet or radiation-driven wind/outflow as the origin of the radio emission.
2. POX 52, along with several other objects, aligns well with the low-mass extension of the fundamental plane for high Eddington ratio, radio-quiet AGNs (Z.-Y. Li et al. 2008). This extension places critical new constraints on BH scaling relations and reinforces the paradigm of self-similar accretion processes across seven orders of magnitude in BH mass. However, approximately half of the other low-mass AGNs with high Eddington ratios deviate from this relationship, emphasizing the need to investigate intrinsic physical processes or potential errors in the measurement of fundamental plane variables.

This study successfully detects radio emission from the IMBH in POX 52 at sub-arcsecond scales, establishing a

critical stepping stone for future investigations at milliarcsecond resolutions. The complementary use of deep, multi-frequency radio imaging with ATCA and VLA has provided valuable insights into the characterization of IMBH properties, offering a solid foundation for exploring similar objects in future studies.

These results can provide a crucial link to broader astrophysical questions and hold significant implications for understanding BH growth and evolution across cosmic time. By characterizing the properties of nearby IMBHs such as POX 52, we uncover critical insights into the origins of BH seeds in the early Universe—a subject of heightened importance in light of recent JWST discoveries of luminous high-redshift quasars. Looking ahead, upcoming facilities—including the next-generation Very Large Array (ngVLA; E. J. Murphy et al. 2018), the Square Kilometre Array (SKA; R. Braun et al. 2019), and the FAST Core Array (P. Jiang et al. 2024)—are poised to play a pivotal role in advancing sensitivity and resolution, enabling transformative breakthroughs in the study of IMBHs and their cosmological implications.

Acknowledgments

We thank the anonymous referee for helpful comments. This work is supported by the National Key R&D Program of China Nos. 2022YFF0503402 and 2023YFA1607903 and the Future Network Partner Program, CAS, No. 018GJHZ2022029FN, Overseas Center Platform Projects, CAS, No. 178GJHZ2023184MI, National Natural Science Foundation of China (NSFC) No. 1247030223. M.F.G. is supported by the National Science Foundation of China (grant 12473019), the National SKA Program of China (grant No. 2022SKA0120102), the Shanghai Pilot Program for Basic Research–Chinese Academy of Science, Shanghai Branch (JCYJ-SHFY-2021-013), and the China Manned Space Project with No. CMSCSST-2021-A06. Q.Y. and M.Z. are supported by the National Key R&D Intergovernmental Cooperation Program of China (2022YFE0133700) and the National Natural Science Foundation of China (12173078). R.Z.S. acknowledges support from the China Postdoctoral Science Foundation (grant No. 2024M752979). N.C. acknowledges support from the Xinjiang Tianchi Talent Program. This work has made use of data from the European Space Agency (ESA) mission Gaia (<https://www.cosmos.esa.int/gaia>) processed by the Gaia Data Processing and Analysis Consortium (DPAC, <https://www.cosmos.esa.int/web/gaia/dpac/consortium>). The Australia Telescope Compact Array is part of the Australia Telescope National Facility (grid.421683.a), which is funded by the Australian Government for operation as a National Facility managed by CSIRO. We acknowledge the Gomeri people as the traditional owners of the Observatory site. The National Radio Astronomy Observatory (NRAO) is a facility of the National Science Foundation operated under cooperative agreement by Associated Universities, Inc. This paper makes use of the VLA data from program 23A-163.















Software: CASA (CASA TEAM ET AL. 2022), RACS-tool.¹³

ORCID iDs

Qi Yuan <https://orcid.org/0000-0003-4671-1740>

Hengxiao Guo <https://orcid.org/0000-0001-8416-7059>

¹³ <https://github.com/alecthomson/RACS-tool>

Minfeng Gu  <https://orcid.org/0000-0002-4455-6946>
 Jamie Stevens  <https://orcid.org/0000-0002-5841-3348>
 Philip G. Edwards  <https://orcid.org/0000-0002-8186-4753>
 Yongjun Chen  <https://orcid.org/0000-0001-5650-6770>
 Wenwen Zuo  <https://orcid.org/0000-0002-4521-6281>
 Jun Yang  <https://orcid.org/0000-0002-2322-5232>
 Paulina Lira  <https://orcid.org/0000-0003-1523-9164>
 Tao An  <https://orcid.org/0000-0003-4341-0029>
 Renzhi Su  <https://orcid.org/0000-0002-2432-2587>
 Yuanqi Liu  <https://orcid.org/0000-0001-9321-6000>
 Yijun Wang  <https://orcid.org/0000-0002-1010-7763>
 Ning Chang  <https://orcid.org/0000-0002-8684-7303>
 Pengfei Jiang  <https://orcid.org/0000-0003-3166-5657>
 Ming Zhang  <https://orcid.org/0000-0002-8315-2848>

References

- Askar, A., Baldassare, V. F., & Mezcua, M. 2023, arXiv:2311.12118
- Baldassare, V. F., Geha, M., & Greene, J. 2018, *ApJ*, **868**, 152
- Bariuan, L. G. C., Snios, B., Sobolewska, M., Siemiginowska, A., & Schwartz, D. A. 2022, *MNRAS*, **513**, 4673
- Barth, A. J., Ho, L. C., Rutledge, R. E., & Sargent, W. L. W. 2004, *ApJ*, **607**, 90
- Bondi, M., Ciliegi, P., Zamorani, G., et al. 2003, *A&A*, **403**, 857
- Braun, R., Bonaldi, A., Bourke, T., Keane, E., & Wagg, J. 2019, arXiv:1912.12699
- CASA Team, Bean, B., Bhatnagar, S., et al. 2022, *PASP*, **134**, 114501
- Chang, N., Xie, F. G., Liu, X., et al. 2021, *MNRAS*, **503**, 1987
- Cho, H., Woo, J.-H., Treu, T., et al. 2021, *ApJ*, **921**, 98
- Clark, B. G. 1980, *A&A*, **89**, 377
- Condon, J. J. 1992, *ARA&A*, **30**, 575
- Connors, R. M. T. 2017, PhD thesis, Univ. Amsterdam Netherlands
- Dong, X.-B., Ho, L. C., Yuan, W., et al. 2012, *ApJ*, **755**, 167
- Falcke, H., K rding, E., & Markoff, S. 2004, *A&A*, **414**, 895
- Filippenko, A. V., & Ho, L. C. 2003, *ApJL*, **588**, L13
- Gaia Collaboration, Vallenari, A., Brown, A. G. A., et al. 2023, *A&A*, **674**, A1
- Gordon, Y. A., Boyce, M. M., O'Dea, C. P., et al. 2021, *ApJS*, **255**, 30
- Greene, J. E., & Ho, L. C. 2004, *ApJ*, **610**, 722
- Greene, J. E., & Ho, L. C. 2006, *ApJ*, **641**, 117
- Greene, J. E., & Ho, L. C. 2007, *ApJ*, **670**, 92
- Greene, J. E., Ho, L. C., & Ulvestad, J. S. 2006, *ApJ*, **636**, 56
- Gudel, M., & Benz, A. O. 1993, *ApJL*, **405**, L63
- G ltekin, K., Cackett, E. M., King, A. L., Miller, J. M., & Pinkney, J. 2014, *ApJL*, **788**, L22
- G ltekin, K., Nyland, K., Gray, N., et al. 2022, *MNRAS*, **516**, 6123
- G ltekin, K., Richstone, D. O., Gebhardt, K., et al. 2009, *ApJ*, **698**, 198
- Ho, L. C. 2002, *ApJ*, **564**, 120
- Ho, L. C., & Ulvestad, J. S. 2001, *ApJS*, **133**, 77
- Huynh, M. T., Jackson, C. A., Norris, R. P., & Prandoni, I. 2005, *AJ*, **130**, 1373
- Inayoshi, K., Visbal, E., & Haiman, Z. 2020, *ARA&A*, **58**, 27
- Jiang, P., Chen, R., Gan, H., et al. 2024, *AstTI*, **1**, 84
- Kamizasa, N., Terashima, Y., & Awaki, H. 2012, *ApJ*, **751**, 39
- Kawamuro, T., Ricci, C., Yamada, S., et al. 2024, *ApJ*, **960**, 15
- Kellermann, K. I., Sramek, R., Schmidt, M., Shaffer, D. B., & Green, R. 1989, *AJ*, **98**, 1195
- Kellermann, K. I., Sramek, R. A., Schmidt, M., Green, R. F., & Shaffer, D. B. 1994, *AJ*, **108**, 1163
- Kennicutt, R. C., & Evans, N. J. 2012, *ARA&A*, **50**, 531
- Kokorev, V., Fujimoto, S., Labbe, I., et al. 2023, *ApJL*, **957**, L7
- Kovalev, Y. Y., Kellermann, K. I., Lister, M. L., et al. 2005, *AJ*, **130**, 2473
- Lacy, M., Baum, S. A., Chandler, C. J., et al. 2020, *PASP*, **132**, 035001
- Laor, A., Baldi, R. D., & Behar, E. 2019, *MNRAS*, **482**, 5513
- Lehmer, B. D., Basu-Zych, A. R., Mineo, S., et al. 2016, *ApJ*, **825**, 7
- Li, Z.-Y., Wu, X.-B., & Wang, R. 2008, *ApJ*, **688**, 826
- Liu, H.-Y., Yuan, W., Dong, X.-B., Zhou, H., & Liu, W.-J. 2018, *ApJS*, **235**, 40
- Ludwig, R. R., Greene, J. E., Barth, A. J., & Ho, L. C. 2012, *ApJ*, **756**, 51
- Maccarone, T. J. 2004, *MNRAS*, **351**, 1049
- Martinez-Palomera, J., Lira, P., Bhalla-Ladd, I., F rster, F., & Plotkin, R. M. 2020, *ApJ*, **889**, 113
- McMullin, J. P., Waters, B., Schiebel, D., Young, W., & Golap, K. 2007, in ASP Conf. Ser. 376, *Astronomical Data Analysis Software and Systems XVI*, ed. R. A. Shaw, F. Hill, & D. J. Bell (San Francisco, CA: ASP), 127
- Merloni, A., Heinz, S., & di Matteo, T. 2003, *MNRAS*, **345**, 1057
- Mezcua, M. 2017, *IJMPD*, **26**, 1730021
- Murphy, E. J., Bolatto, A., Chatterjee, S., et al. 2018, in ASP Conf. Ser. 517, *Science with a Next Generation Very Large 763 Array*, ed. E. Murphy (San Francisco, CA: ASP), 3
- Murphy, E. J., Bremseth, J., Mason, B. S., et al. 2012, *ApJ*, **761**, 97
- Murphy, E. J., Condon, J. J., Schinnerer, E., et al. 2011, *ApJ*, **737**, 67
- Nandi, P., Stalin, C. S., Saikia, D. J., et al. 2023, *ApJ*, **959**, 116
- Pandey, S., Rakshit, S., Chand, K., et al. 2024, *ApJ*, **976**, 116
- Panessa, F., Baldi, R. D., Laor, A., et al. 2019, *NatAs*, **3**, 387
- Panessa, F., Barcons, X., Bassani, L., et al. 2007, *A&A*, **467**, 519
- Raginski, I., Chiaraluce, E., Bruni, G., et al. 2022, *MNRAS*, **515**, 473
- Panessa, F., & Giroletti, M. 2013, *MNRAS*, **432**, 1138
- Paul, J. D., Plotkin, R. M., Brandt, W. N., et al. 2024, *ApJ*, **974**, 66
- Perley, R. A., & Butler, B. J. 2017, *ApJS*, **230**, 7
- Plotkin, R. M., Markoff, S., Kelly, B. C., K rding, E., & Anderson, S. F. 2012, *MNRAS*, **419**, 267
- Prandoni, I., Gregorini, L., Parma, P., et al. 2000, *A&AS*, **146**, 31
- Qian, L., Dong, X.-B., Xie, F.-G., Liu, W., & Li, D. 2018, *ApJ*, **860**, 134
- Raginski, I., & Laor, A. 2016, *MNRAS*, **459**, 2082
- Reines, A. E., Condon, J. J., Darling, J., & Greene, J. E. 2020, *ApJ*, **888**, 36
- Reines, A. E., Greene, J. E., & Geha, M. 2013, *ApJ*, **775**, 116
- Saikia, P., K rding, E., Coppejans, D. L., et al. 2018, *A&A*, **616**, A152
- Salehirad, S., Reines, A. E., & Molina, M. 2022, *ApJ*, **937**, 7
- Sargent, A. J., Johnson, M. C., Reines, A. E., et al. 2022, *ApJ*, **933**, 160
- Sartori, L. F., Schawinski, K., Treister, E., et al. 2015, *MNRAS*, **454**, 3722
- Satyapal, S., Secrest, N. J., McAlpine, W., et al. 2014, *ApJ*, **784**, 113
- Sault, R. J., Teuben, P. J., & Wright, M. C. H. 1995, in ASP Conf. Ser. 77, *Astronomical Data Analysis Software and 807 Systems IV*, ed. R. A. Shaw, H. E. Payne, & J. J. E. Hayes (San Francisco, CA: ASP), 443
- Shen, Y. 2013, *BASI*, **41**, 61
- Shimwell, T. W., Hardcastle, M. J., Tasse, C., et al. 2022, *A&A*, **659**, A1
- Shimwell, T. W., R ttgering, H. J. A., Best, P. N., et al. 2017, *A&A*, **598**, A104
- Shimwell, T. W., Tasse, C., Hardcastle, M. J., et al. 2019, *A&A*, **622**, A1
- Stern, D., Assef, R. J., Benford, D. J., et al. 2012, *ApJ*, **753**, 30
- Terashima, Y., & Wilson, A. S. 2003, *ApJ*, **583**, 145
- Thompson, A. R., Clark, B. G., Wade, C. M., & Napier, P. J. 1980, *ApJS*, **44**, 151
- Thornton, C. E., Barth, A. J., Ho, L. C., Rutledge, R. E., & Greene, J. E. 2008, *ApJ*, **686**, 892
- Valiante, R., Schneider, R., Graziani, L., & Zappacosta, L. 2018, *MNRAS*, **474**, 3825
- van Wassenhove, S., Volonteri, M., Walker, M. G., & Gair, J. R. 2010, *MNRAS*, **408**, 1139
- Visnovsky, K. L., Impey, C. D., Foltz, C. B., et al. 1992, *ApJ*, **391**, 560
- Volonteri, M., Lodato, G., & Natarajan, P. 2008, *MNRAS*, **383**, 1079
- Wang, A., An, T., Zhang, Y., et al. 2023, *MNRAS*, **525**, 6064
- Wang, R., Wu, X.-B., & Kong, M.-Z. 2006, *ApJ*, **645**, 890
- Wang, Y., Wang, T., Ho, L. C., Zhong, Y., & Luo, B. 2024, *A&A*, **689**, A327
- Wasleske, E. J., & Baldassare, V. F. 2024, *ApJ*, **971**, 68
- Wilson, W. E., Ferris, R. H., Axtens, P., et al. 2011, *MNRAS*, **416**, 832
- Woo, J.-H., Cho, H., Gallo, E., et al. 2019, *NatAs*, **3**, 755
- Wu, J.-Z., Dong, X.-B., Qian, L., et al. 2024, *ApJS*, **271**, 64
- Yang, J., Paragi, Z., Frey, S., et al. 2023, *MNRAS*, **520**, 5964
- Yang, J., Yang, X., Wrobel, J. M., et al. 2022, *MNRAS*, **514**, 6215
- Yang, X., & Yang, J. 2023, *Galax*, **11**, 53
- Yuan, F., Yu, Z., & Ho, L. C. 2009, *ApJ*, **703**, 1034